Undersampling correction for array detector-based satellite spectrometers

Kelly Chance, Thomas P. Kurosu, and Christopher E. Sioris

Array detector-based instruments are now fundamental to measurements of ozone and other atmospheric trace gases from space in the ultraviolet, visible, and infrared. The present generation of such instruments suffers, to a greater or lesser degree, from undersampling of the spectra, leading to difficulties in the analysis of atmospheric radiances. We provide extended analysis of the undersampling suffered by modern satellite spectrometers, which include the Global Ozone Monitoring Experiment, Scanning Imaging Absorption Spectrometer for Atmospheric Chartography, Ozone Monitoring Instrument, and Ozone Mapping and Profiler Suite. The analysis includes basic undersampling, the effects of binning into separate detector pixels, and the application of high-resolution Fraunhofer spectral data to correct for undersampling in many useful cases.

OCIS codes: 010.1280, 120.4570, 280.1120.

1. Introduction

Array-based spectrometers used in atmospheric remote sensing can suffer substantially from spectral undersampling, with negative consequences to the quality of data retrieved from the measurements. This circumstance was first obvious in measurements from the Global Ozone Monitoring Experiment (GOME),[1] in which scientists fitting trace gases from GOME spectra found large systematic fitting residuals, and large fitting errors, even after correcting for Doppler shifts between radiances and irradiances. In a previous study it was recognized that this result was mainly due to spectral undersampling, and a technique was presented for correcting most (>90%) of the *undersampling error* in spectral regions where atmospheric absorption effects are small.[2] For GOME, this includes fitting regions used for nitrogen dioxide (NO_2), bromine monoxide (BrO), chlorine dioxide (OClO), and formaldehyde (HCHO). If used with caution, the technique can also be applied successfully to ozone (O_3) and sulfur dioxide (SO_2). (Caution is required because the absorption optical depths for O_3 are higher than for the other trace species listed; correction assumes that, to first order, the radiance spectrum consists mostly of backscattered Fraunhofer structure. The SO_2 absorption occurs in the region where O_3 also absorbs strongly.) The technique consists of comparing fully sampled and undersampled versions of a high-resolution Fraunhofer reference spectrum,[3] with the difference being the effect of undersampling. Slijkhuis *et al.*[4] suggested that the observed residuals are induced by the resampling needed to compare Earth radiance and solar irradiance spectra in the fitting, because they are measured with different Doppler shifts of the ERS-2 satellite with respect to the sun. It is demonstrated here that this is not entirely the case: Wavelength shifts between GOME radiances and irradiances are larger than can be accounted for by Doppler shifts. Slijkhus *et al.*[4] also presented a version of the technique (see Ref. 2) implemented in the Scanning Imaging Absorption Spectrometer for Atmospheric Chartography (SCIAMACHY) operational processor. The technique is now also used for measurement of HCHO[5] and NO_2[6] and has been implemented in the operational processor for measurements of BrO, OClO, and HCHO by the Ozone Monitoring Instrument (OMI).[7]

The present analysis improves on the previous understanding of correction for undersampling because the sampling theorem in conjunction with the instrument slit function is fully considered. The analysis is applied to measurements by GOME and OMI, since they represent the two major instrument types: diode array detectors (GOME) and CCD detectors (OMI). The development applies as well to other instruments, including SCIAMACHY (diode array detectors) and

K. Chance (kchance@cfa.harvard.edu), T. P. Kurosu, and C. E. Sioris are with the Harvard-Smithsonian Center for Astrophysics, Mail Stop 50, 60 Garden Street, Cambridge, Massachusetts, 02138-1596.

Received 7 January 2004; revised manuscript received 12 August 2004; accepted 27 September 2004.

0003-6935/05/071296-09$15.00/0

the Ozone Mapping and Profiler Suite (OMPS), part of the National Polar Orbiting Environmental Satellite System, which uses CCD detectors.

2. Definitions and Assumptions

The spectrometers considered here use array detectors, which respond to the incoming light over finite regions, with defined response profiles. We will use the term instrument line shape (ILS) for the response of a spectrometer to a monochromatic source up to where it enters the array detector and the term instrument transfer function (ITF) for the ILS convolved with the detector pixel response. The following properties are assumed to be valid over the region of the array detector that is necessary to consider for ITFs and undersampling corrections at a given pixel, as developed here.

1. **Linear response.** Each pixel responds linearly to input light intensity.
2. **Equal pixel response.** Pixels respond equally to photons of different wavelength. Pixels respond (or can be calibrated to respond) equally in output signal for equal input light intensity.
3. **Linear dispersion.** Pixel wavelengths are at equal increments.
4. **No end-point issues.** The region under consideration is sufficiently far from the array end for wavelengths beyond the array wavelength range to contribute to the signal. (Proximity to the array end would require recalculation of the ILS from deconvolution of the ITF, as discussed below.)
5. **Calibration light source issues.** ITFs are determined using either
   - lines with negligible spectral width or
   - a tunable source with negligible spectral width and equal intensity as it is tuned over the ITF.
6. **Slit width variation** is negligible over the ITF centered at each particular wavelength.

Higher-order corrections will likely be needed in the future to account for the breakdown of some of these assumptions.

3. Spectral Undersampling

Consider a wavelength range extending from λ_{min} to λ_{max} that is fully or partly sampled by an array of detectors, spaced at wavelength increment $\delta\lambda$. Any continuous incoming signal spectrum extending over the wavelength range can be represented fully by expansion in spatial (i.e., wavelength) frequency in a Fourier series

$$\begin{aligned} S(\lambda) &= a_0 + \sum_{k=1}^{\infty} [a_k \cos kt + b_k \sin kt] \\ &= a_0 + \sum_{k=1}^{\infty} \{a_k \cos[\omega_k(\lambda - \lambda_{min})] \\ &\quad + b_k \sin[\omega_k(\lambda - \lambda_{min})]\}, \end{aligned} \tag{1}$$

where

$$t = 2\pi \frac{\lambda - \lambda_{min}}{\lambda_{max} - \lambda_{min}} \equiv 2\pi \frac{\lambda - \lambda_{min}}{\Delta\lambda}, \tag{2}$$

and the spatial frequencies are

$$\omega_k = \frac{2\pi k}{\Delta\lambda}. \tag{3}$$

Suppose that the signal is band limited, that is, limited in content of spatial frequency components to a maximum spatial frequency ω_{max}. Then, by the sampling theorem,[8,9] the information content of the spectrum is fully known if the spectrum is sampled over the full range λ_{min} to λ_{max} to twice this maximum spatial frequency, $2\omega_{max}$ (the Nyquist-sampling frequency):

$$\frac{\delta\lambda}{2\pi} = \frac{1}{2\omega_{max}}. \tag{4}$$

In this case, the signal expansion includes only the terms necessary to measure spatial frequencies $\leq\omega_{max}$:

$$S(\lambda) = a_0 + \sum_{k=1}^{N} [a_k \cos kt + b_k \sin kt], \qquad N = \frac{\Delta\lambda}{2\delta\lambda}. \tag{5}$$

The spectrum is completely determined by this expansion. Its values at points other than the sampled points can be determined by the fact that the value at each sampled point λ_n represents the intensity c_n of a sampling function, $\mathrm{sinc}[2\pi(\lambda_n - \lambda)/\delta\lambda]$, centered at that point,[8]

$$\mathrm{sinc}[2\pi(\lambda_n - \lambda)/\delta\lambda] = \frac{\sin[2\pi(\lambda_n - \lambda)/\delta\lambda]}{[2\pi(\lambda_n - \lambda)/\Delta\lambda]}, \tag{6}$$

plus the constant offset a_0:

$$\begin{aligned} c_n &= S(\lambda_n) - a_0 = \sum_{k=1}^{N} [a_k \cos kt_n + b_k \sin kt_n], \\ t_n &= \frac{2\pi(\lambda_n - \lambda_{min})}{\Delta\lambda}. \end{aligned} \tag{7}$$

The sampling function is written here in this way to emphasize the pixel dependence and orientation of the following discussion. The sampling function presented here is actually an approximation to a fuller and more complex form,[9,10] but the difference amounts to a completely negligible correction except within several sample points of the λ_{min} and λ_{max} end points.

If the signal is not band limited to ω_{max} but is still sampled to only $2\omega_{max}$, spatial frequencies greater than ω_{max} are aliased into the band $0 < \omega \leq \omega_{max}$, with signal information for $\omega_{max} < \omega \leq 2\omega_{max}$ appearing

at $\omega_{max} - \omega$ and information for $2\omega_{max} < \omega \leq 3\omega_{max}$ appearing at $\omega - 2\omega_{max}$, etc. (Ref. 9, pp. 16–18). It will be demonstrated in Section 4 that information aliased from the spatial frequency band $\omega_{max} < \omega \leq 2\omega_{max}$ represents the most important sources of problems for GOME and the main target of corrections. Problems from aliasing in the spectra become most evident when it becomes necessary to resample a spectrum in wavelength, for example, when comparing an atmospheric radiance spectrum with a solar irradiance spectrum to determine atmospheric composition from molecular absorption lines, but the interference from aliasing is present in any case when the spectrum is undersampled (i.e., the spectrum is not fully Nyquist sampled). For example, synthetic spectra calculated during the fitting process to determine abundances of atmospheric gases would not normally include aliasing, whereas the measured spectra would.

A Nyquist-sampled spectrum $S(\lambda)$ is fully described by summing over the contributions from the m individual sample points

$$S(\lambda) = c_0 + \sum_{i=1}^{m} c_i \, \mathrm{sinc}[2\pi(\lambda_i - \lambda)/\delta\lambda], \tag{8}$$

where $m = 2N = \Delta\lambda/\delta\lambda$. It is now possible to investigate the case in which the spectrum is not fully Nyquist sampled. Consider a spectrum input to the instrument $S_{inp}(\lambda)$. If the spectrum is completely known *a priori,* it can be expanded as before in a Fourier series

$$S_{inp}(\lambda) = a_0 + \sum_{k=1}^{\infty} [a_k \cos kt + b_k \sin kt]. \tag{9}$$

S_{inp} can be separated into a Nyquist-sampled part, S_{Nyq}, containing only spatial frequencies $\leq \omega_{max}$, and an undersampled part, S_{und}

$$S_{Nyq}(\lambda) = a_0 + \sum_{k=1}^{N} [a_k \cos kt + b_k \sin kt], \tag{10a}$$

$$S_{und}(\lambda) = \sum_{k=N+1}^{\infty} [a_k \cos kt + b_k \sin kt]. \tag{10b}$$

The undersampled part of the spectrum is thus

$$S_{und}(\lambda) = S_{inp}(\lambda) - \sum_{i=1}^{m} c_i \, \mathrm{sinc}[2\pi(\lambda_i - \lambda)/\delta\lambda] - c_0, \tag{11}$$

where m runs over the sampled points.

4. Slit Functions (Instrument Transfer Functions)

An ITF serves as a low-pass filter to limit the spatial frequency content of the spectrum. Ideally, an ITF would limit the spectral information to frequencies $\leq \omega_{max}$. The ITFs for satellite-based spectrometers are measured in one of three manners:

1. By use of a reference line lamp (often a PtNeCr lamp[11]). This method has the advantage that lamp lines are much narrower than the ITF. The disadvantages are that lines are not always completely separated, that spectral coverage may be inadequate in some regions, and that a set of points (one per detector pixel) is mapped out, rather than a continuous ITF. This method was used for GOME and SCIAMACHY.
2. By use of a tunable source consisting of a broadband light source and a monochromator. This method has the advantage of mapping out a continuous ITF but the disadvantage of being a spectrally broader source than the PtNeCr line source. This method was used for OMI, where the full-width at half-maximum (FWHM) of the source was ≤ 0.1 OMI detector pixel.[12] The residual effects from finite source width could, in principle, be reduced by use of the deconvolution techniques introduced in Section 5.
3. By fitting of flight spectral irradiance data to a high-resolution solar reference spectrum,[3] for which the fitting includes wavelength adjustment and simultaneous fitting to a parameterized ITF.[2,13]

An ITF, $\Gamma(\lambda)$, can be expanded to include Nyquist-sampled and undersampled portions, if one ignores (for now) detector pixel binning:

$$\Gamma(\lambda) = \gamma_0 + \sum_{i=a}^{b} \gamma_i \, \mathrm{sinc}[2\pi(\lambda_i - \lambda)/\delta\lambda] + \Gamma_{und}(\lambda). \tag{12}$$

The limits a and b are selected to include portions of the detector array where the slit function contributes significantly. As examples, we show the Gaussian GOME ITF we normally use for wavelength calibration purposes. A more complex, compound hypergeometric ITF was determined during the instrument characterization.[14] We find that the Gaussian spectrum provides better wavelength calibration for GOME spectra, and we use it routinely in our data analyses. It also provides much better undersampling correction for GOME spectral fitting. We show an OMI ITF (see Ref. 12) for this same wavelength region and for the NO_2 fitting region (405–465 nm; the ITF determined at 432 nm is used here). The OMI ITFs are selected for CCD row 150, corresponding to a viewing azimuth angle of 29.5°, approximately halfway from the nadir view to the extremity of the OMI swath. Additional types of ITFs for OMI may be considered once there is flight data for comparison. For all ITFs shown in this section, the complication of binning over the detector pixel response function is not yet included. This complication will be discussed in Section 5.

Figure 1 shows the GOME Gaussian ITF, determined from ERS-2 orbit 81003031 (3 October 1998), used here as a test orbit for determination of undersampling correction, appropriate to the fitting win-

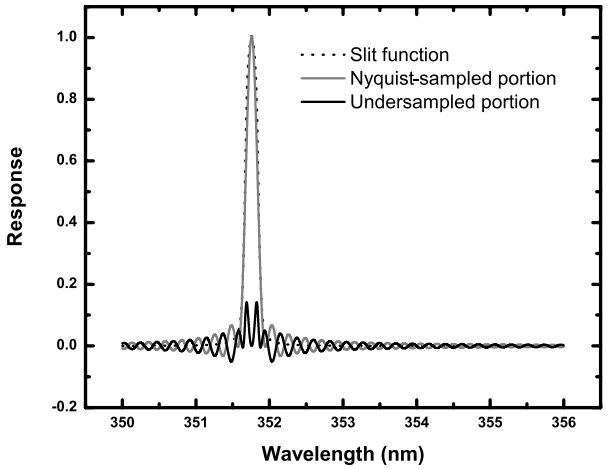

Fig. 1. GOME Gaussian ITF in the spectral region used for BrO determinations, and its decomposition into Nyquist-sampled and undersampled components.

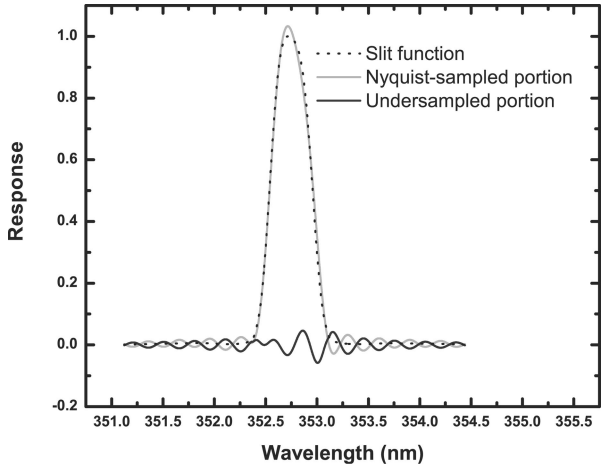

Fig. 3. OMI ITF for the BrO fitting region and the Nyquist-sampled and undersampled portions.

dow used for BrO retrieval in GOME.[2] The FWHM of the ITF is 0.160 nm, and there are 1.4 samples per FWHM in this region of GOME spectra. The ITF is additionally decomposed into fully sampled and undersampled components. Figure 2 shows this ITF with the hypothetical sampling to twice the GOME sampling frequency. Figure 3 shows the OMI ITF for this same wavelength region (FWHM = 0.421 nm, 2.8 samples per FWHM) and its decomposition into fully sampled and undersampled components. Figure 4 shows this ITF with the hypothetical sampling to twice the OMI sampling frequency. Figures 5 and 6 show the OMI ITFs and decompositions for the NO_2 fitting wavelength range (FWHM = 0.639 nm, 3.0 samples per FWHM). Note the asymmetry in the measured OMI ITFs and their decompositions.

It is clear from all three examples that higher sampling by a factor of 2 greatly decreases the undersampled portion of the ITF, almost eliminating undersampling. Since for GOME this sampling corresponds to 2.8 samples per FWHM, this result demonstrates that information aliased from the spatial frequency band $\omega_{max} < \omega \leq 2\omega_{max}$ represents the most important source of undersampling in this spectral region.

5. Binning into Detector Pixels

GOME and SCIAMACHY use Reticon-S RL-1024 SRU-type linear diode array detectors, which are designed to have the sensitivity profiles shown in Fig. 7 for the spectral resolution and sampling of GOME. These detectors have 1024 photodiode elements spaced at 25 μm . The center 13 μm of each element is *n* doped, with the bulk of the material *p* doped, to generate the response profile shown (the newer Reticon-L detectors are also spaced at 25 μm but with 19-μm *n*-doped regions and 6-μm interdiode gaps).

Characterization of the actual pixel responses must take into account that the input light source

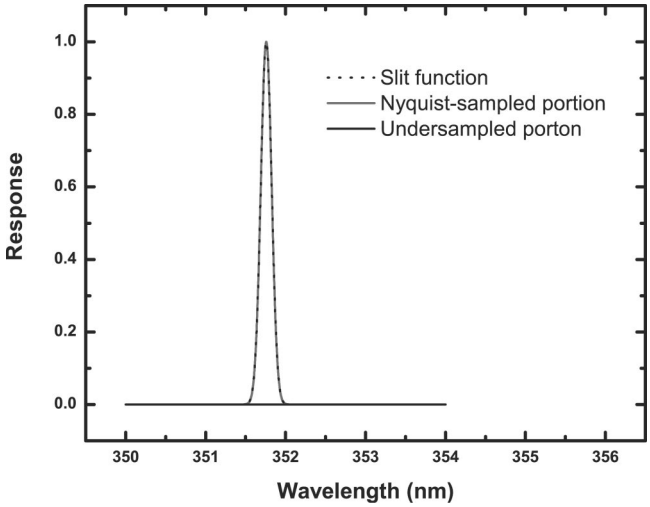

Fig. 2. GOME Gaussian ITF and the Nyquist-sampled and undersampled portions for the hypothetical case in which the slit function is sampled to twice the GOME spatial frequency.

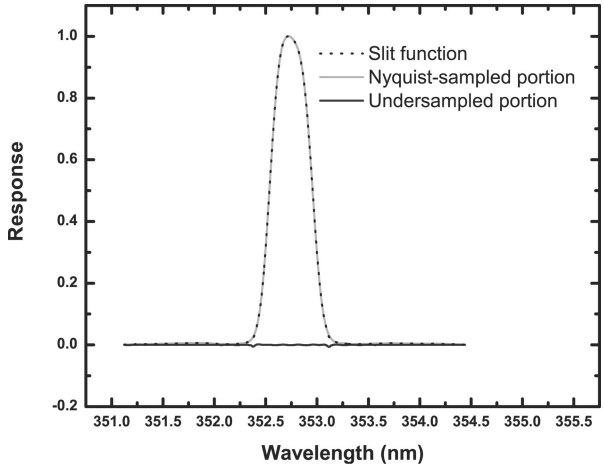

Fig. 4. OMI ITF for the BrO fitting region and the Nyquist-sampled and undersampled portions for the hypothetical case in which the slit function is sampled to twice the OMI spatial frequency.

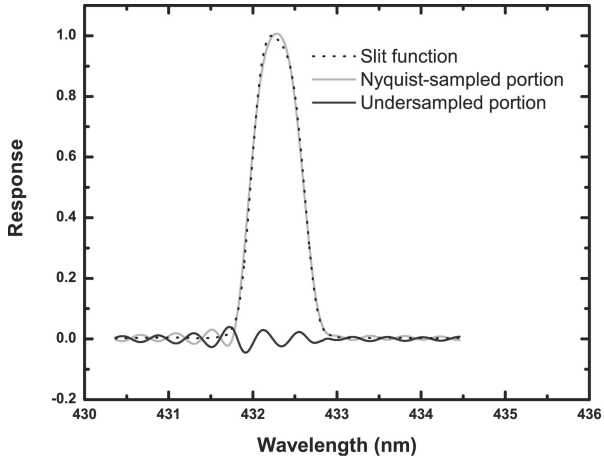

Fig. 5. OMI ITF for the NO_2 fitting region and the Nyquist-sampled and undersampled portions.

(mostly Fraunhofer spectrum, convolved with the ILS) varies significantly across the detector pixel profile. The final response is the integral across the pixel profile of the convolution of the input spectrum with the ILS

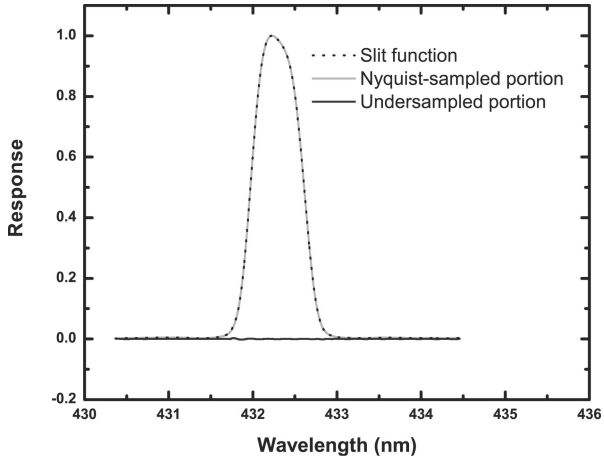

Fig. 6. OMI instrument transfer function for the NO_2 fitting region and the Nyquist-sampled and undersampled portions for the hypothetical case where the slit function is sampled to twice the OMI spatial frequency.

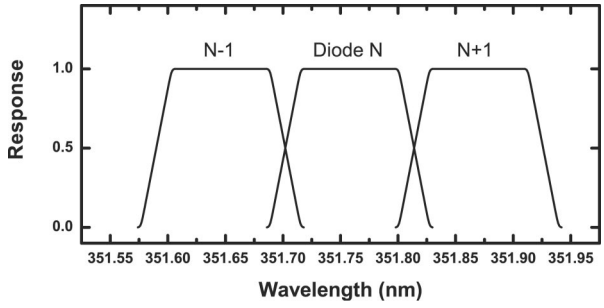

Fig. 7. Response of three Reticon-S detector pixels as a function of location in GOME detector channel 2.

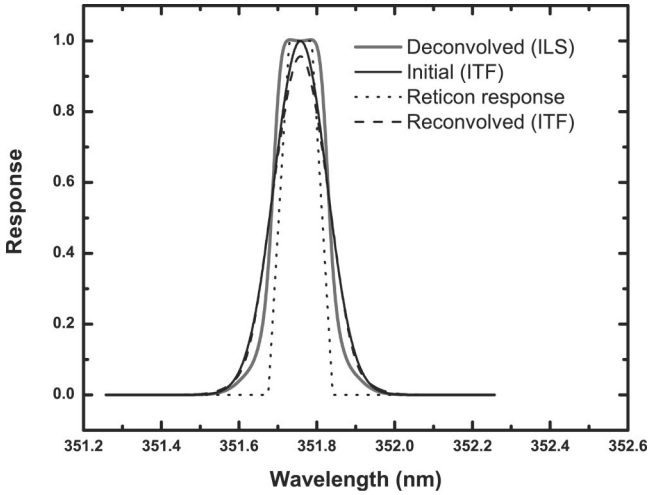

Fig. 8. Deconvolution of the GOME ITF from the pixel response function to determine the ILS in the BrO fitting region.

$$R_{\mathrm{pix}}(\lambda) = \int_{\mathrm{profile}} S(\lambda') \otimes \Gamma(\lambda - \lambda')\mathrm{d}\lambda', \qquad (13)$$

where R_{pix} is the pixel response, S is the input spectrum, Γ is the ILS, and $\otimes$ denotes convolution. To calculate the response, it is first necessary to obtain the ILS by deconvolution, since the measured ITF is the convolution of the ILS with the pixel response profile. This response is accomplished with the Jansson method, as described by Blass and Halsey,[15] for GOME, and a nonlinear least-squares fitting to a parameterized profile shape for OMI. The result for the GOME slit function is shown in Fig. 8. The deconvolved slit is the best match to the ILS that could be obtained in the iterative deconvolution process. The difference between the initial and the reconvolved slit is an indicator of the goodness-of-fit for this procedure. The response functions for the OMI CCD detectors are Gaussian with a FWHM of 25 μm and separated by 22.5 μm.[12] Figures 9 and 10 show

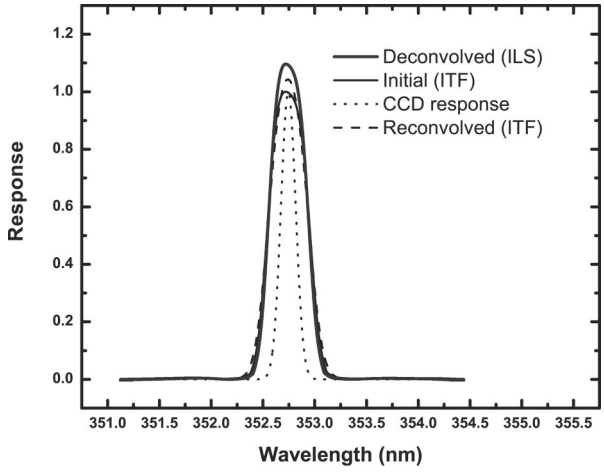

Fig. 9. Deconvolution of the OMI ITF from the pixel response function to determine the ILS in the BrO fitting region.

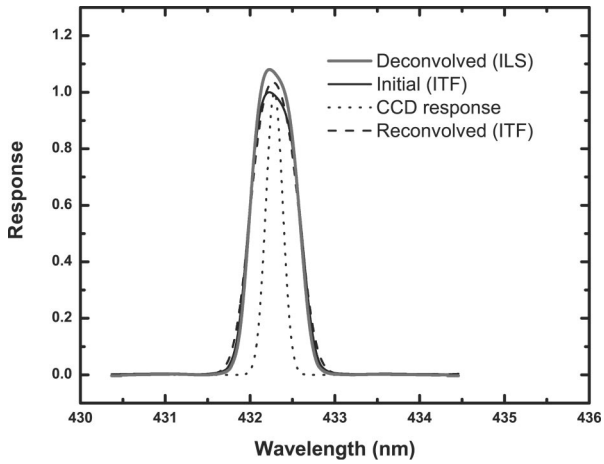

Fig. 10. Deconvolution of the OMI ITF from the pixel response function to determine the ILS in the NO_2 fitting region.

these along with the decomposition to determine the ILS for the BrO and NO_2 fitting regions of OMI.

6. Undersampling Correction

A. Wavelength Calibration Issues

Satellite radiances and irradiances can be calibrated in wavelength with high absolute accuracy (typically ≤ 0.0004 nm for the GOME BrO fitting region) by use of cross correlation to the solar spectrum described by Chance and Spurr,[3] with simultaneous fitting of the ITF.[2,13] Previously it was suggested that the apparent wavelength shift between GOME radiances and irradiances was due to instrumental effects, influencing the way the detectors are illuminated in the different measuring geometries.[2] Slijkhus *et al.*[4] stated that the shift is due to the Doppler effect, since irradiances are obtained during the portion of the orbit when the satellite is moving toward the sun. For ERS-2 orbit 81003031, the maximum velocity toward the sun is 7.46 km s^{-1}, whereas the average wavelength shift (irradiance − radiance) for the BrO fitting window is equivalent to 7.865 ± 0.025 km s^{-1} (0.000923 ± 0.00003 nm). The satellite Doppler shift contributes 6.89 km s^{-1} (0.0081 nm), rather than the full 7.46 km s^{-1}, given the GOME solar measurement procedure.[4] There is an additional component of 0.50 km s^{-1} at this season from the ellipticity of the Earth's orbit, for a total Doppler shift of 7.39 km s^{-1}, leaving a significant instrument, a spectral component, or both (see the discussion in Ref. 16 for possible spectral tilt contributions). For the other spectrometers considered here, the relative contributions are not yet determined. For OMI in particular, since its undersampling is calculated here, a relative shift equal to the full Doppler shift is assumed; this assumption will be modified when flight data become available.

B. Undersampling Calculations

Calculation of the undersampling correction for each case is accomplished by convolution of the high spectral resolution (0.01 nm) solar reference spectrum, described by Chance and Spurr,[3] with the ITF determined for the instrument and wavelength region and by means of differencing fully sampled and undersampled representations of this convolved solar spectrum at the sampling grid of the satellite radiances.

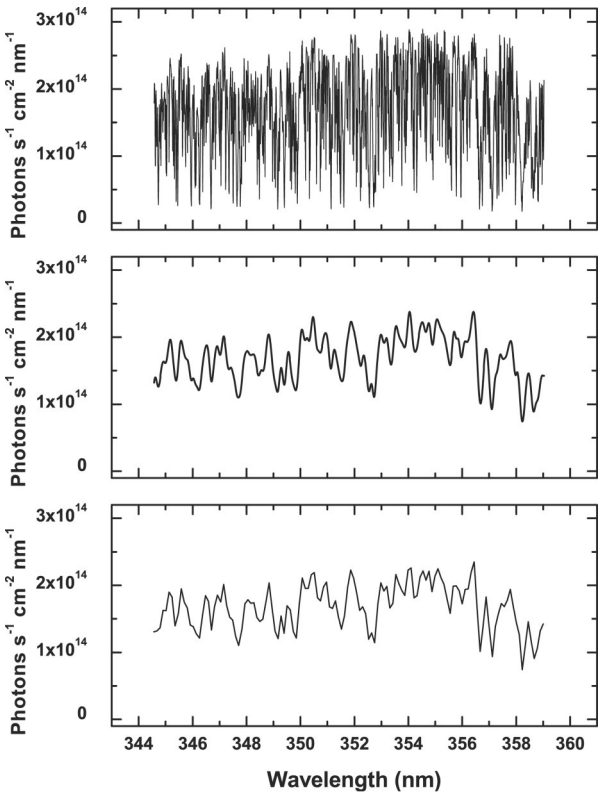

Fig. 11. Portion of the high-resolution solar reference spectrum E_{ref} used in fitting BrO for GOME (top); E_{ref} convolved with the GOME ITF to create the lower spectral resolution but highly oversampled, solar reference spectrum, E_{over} (middle); E_{over} sampled at the wavelength grid of the GOME irradiance (E_{irr}) (bottom). E_{irr} and E_{rad} (not plotted here; see text) are undersampled representations of the solar reference spectrum.

1. Convolve the high-resolution solar reference spectrum E_{ref} with the satellite instrument ITF to create a lower spectral resolution, but a highly oversampled, solar reference spectrum, E_{over},

$$E_{over}(\lambda) = \int_{profile} E_{ref}(\lambda') \otimes \mathrm{ITF}(\lambda - \lambda')\mathrm{d}\lambda'. \quad (14)$$

The portion of E_{ref} used in fitting BrO for GOME is shown in Fig. 11, top panel; E_{over} for this spectral region is shown in Fig. 11, middle panel.

2. Determine from direct cross correlation (for GOME) or by an estimate (for OMI) the wavelength grids for irradiance and radiance spectra g_{irr} and g_{rad}.

3. Sample E_{over} at the wavelength grid g_{irr}, to give E_{irr}, and at the grid g_{rad}, to give E_{rad}, using cubic spline interpolation[17] to determine values at each exact grid point. These are now undersampled representations of the solar reference spectrum, although each is cor-

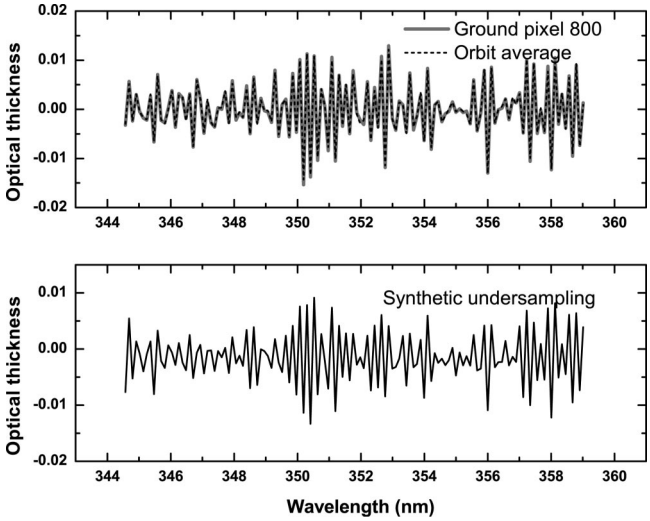

Fig. 12. Residuals from fitting GOME spectra for BrO in ERS-2 orbit 81003031, for a single spectrum and as an average for all spectra in the orbit (top); Synthetic undersampling, C_u, calculated here for the relative wavelength shift between the GOME irradiance and the GOME radiance (bottom).

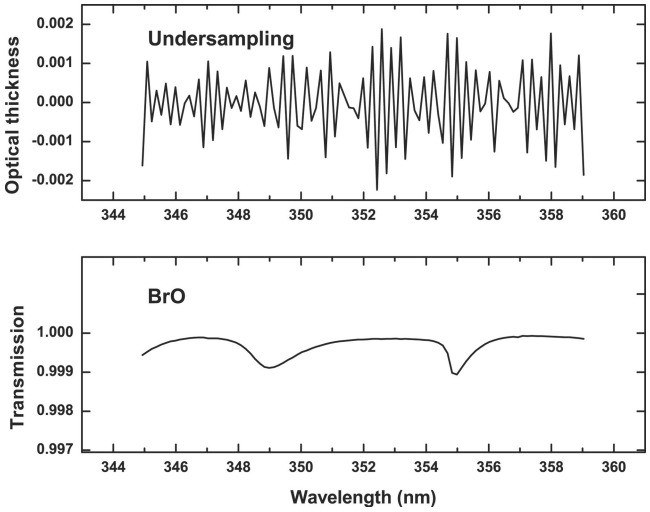

Fig. 13. Synthetic OMI undersampling, C_u, in the BrO fitting region, calculated here for a relative wavelength shift of the irradiance and radiance corresponding to 7.5 km s^{-1} (top); absorption for a typical BrO slant column density of 1×10^{14} cm^{-2} (bottom).

rect at the points on its sampling grid. E_{rad} is shown in Fig. 11, bottom panel; E_{rad} is virtually indistinguishable when overplotted.

4. Resample E_{irr} to the wavelength grid g_{rad}, using cubic spline interpolation, giving E'_{rad}.

5. The undersampling correction C_u, in optical thickness units, is the difference between E_{rad} and E'_{rad}, normalized to the average of E_{rad} over the fitting window:

$$C_u(\lambda) = \frac{E_{rad}(\lambda) - E'_{rad}(\lambda)}{\bar{E}_{rad}}. \quad (15)$$

C_u corresponds to differencing fully sampled and undersampled representations of the convolved solar spectrum since only E_{irr} is resampled, thus inducing undersampling error on the radiance wavelength grid g_{rad}. This undersampling correction assumes that, to first order, the radiance spectrum consists mostly of backscattered Fraunhofer structure. Higher-order corrections could be made to account for atmospheric absorption and the Ring effect. Figure 12 shows the residuals from fitting for BrO (without the use of an undersampling spectrum as a basis function) in ERS-2 orbit 81003031 for a measurement pixel midway through the orbit (pixel 800) and as an orbit average (top panel); the bottom panel shows the undersampling C_u calculated here for the average relative wavelength shift between irradiance and radiance fitted for this orbit (0.0092 nm). The calculated undersampling correction accounts for more than 90% of the fitting residuals. Figure 13, top panel, shows the undersampling calculated for the OMI baseline BrO fitting window, assuming a relative radiance–irradiance shift corresponding to the full Doppler shift for the Aura orbit (7.5 km s^{-1}). The bottom panel shows the absorption for a typical BrO slant column density of 1×10^{14} cm^{-2}. The units (optical thickness and transmission) are equivalent in scale for these small interferences and absorptions. The undersampling correction is roughly an order of magnitude smaller than for GOME but is still larger than the BrO absorption and needs to be carefully included in the fitting of the satellite data. Figure 14, top panel, shows the undersampling calculated for the OMI baseline NO_2 fitting window, assuming a relative radiance–irradiance shift corresponding to the full Doppler shift for the Aura orbit. The bottom panel shows the absorption for a typical NO_2 North American summer slant column density of 1.25×10^{16} cm^{-2}. The contribution is less severe but, at ca. 20% of the nominal NO_2 signal, it is still by no

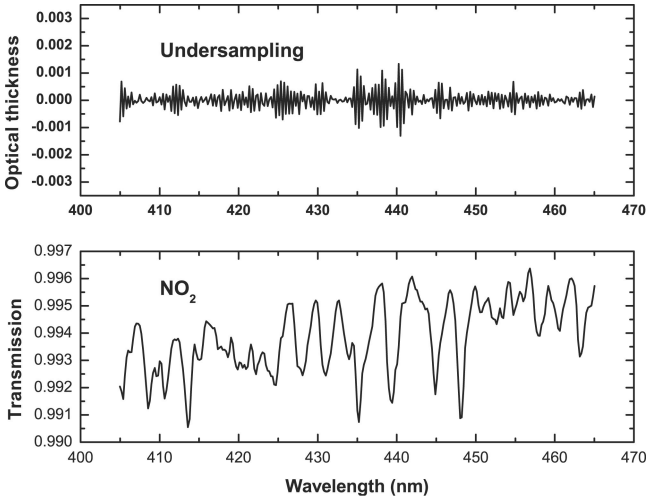

Fig. 14. Synthetic OMI undersampling, C_u, in the NO_2 fitting region, calculated here for a relative wavelength shift of the irradiance and radiance corresponding to 7.5 km s^{-1} (top); absorption for a typical NO_2 slant column density of 1.25×10^{16} cm^{-2} (bottom).

means negligible. Undersampling correction will very likely need to be included to derive meaningful tropospheric NO_2 abundances from OMI measurements. Under heavily polluted conditions over North America in summertime, for example, the tropospheric contribution to the NO_2 slant column usually does not exceed 40%.[6] Effective monitoring of moderate pollution requires correction to substantially better than that level.

An attempt was made to improve the undersampling correction for GOME by calculation of the undersampling spectrum for the deconvolved ILS, followed by convolution of the resulting spectrum with the Reticon response function. The result of this procedure was expected to be an improved undersampling correction that would correspond even more closely to the GOME fitting residual, as shown in Fig. 12, top panel. The actual result was substantially worse. The magnitude was approximately correct, but the spectral details were not. We think that the reason is that the actual detector response function deviates considerably from the trapezoidal shape shown in Fig. 7. For the present, at least, the best undersampling corrections continue to be those determined with the entire ITF. These are shown in Figs. 12–14. When OMI flight data become available, this procedure will be attempted to see whether it provides improved undersampling correction for this case.

7. Discussion and Conclusions

We provide a method that may be used to simply and reliably estimate the degree of undersampling an instrument configuration will have. For instruments in which the ITF may be approximated as Gaussian (GOME), we show that sampling at 2.8 pixels/FWHM will almost completely eliminate undersampling. For more complex ITFs (OMI), significant undersampling can exist at 3.0 pixels/FWHM.

Undersampling for ground-based, zenith-sky spectrometers has been discussed in Ref. 18 in the context of measuring O_2, NO_2, and NO_3. On the basis of numerical experiments, it is recommend to use sampling ratios between 4.5 and 6.5 pixels/FWHM, for Gaussian ITFs, to avoid undersampling. This recommendation is consistent with our finding that for OMI NO_2 measurements undersampling will be significant and will highly affect tropospheric NO_2 measurements at 3.0 pixels/FWHM, but that at 6.0 pixels/FWHM, it becomes negligible. The improvement in undersampling of OMI over that of GOME is due to the higher sampling rates (2.8 and 3.0 samples per FWHM for the OMI UV and visible examples versus 1.4 for the GOME UV example). Asymmetric ITFs such as those of OMI and perhaps other imaging spectrometers may require higher sampling ratios than symmetric ITFs.

The previously developed undersampling correction[2,4] is now commonly used in GOME scientific analyses and has been implemented operationally for SCIAMACHY. It has been demonstrated here that correction will be required for OMI BrO and tropospheric NO_2 measurements, at least. Complete implementation will not be possible until the ITFs and irradiance–radiance wavelength shifts are characterized in flight versus CCD row. A similar conclusion almost certainly applies to the OMPS instruments.

Further refinement of the undersampling correction for OMI, to include full averaging of the solar spectrum over the ILS and convolution with the pixel response, is currently in progress, to be ready for application to flight spectra. For GOME, this further refinement has been shown not to be an improvement, likely because of incorrect characterization of the Reticon response function. Convolution with the ITF followed by the sampling procedure described above in Subsection 6.B provides very accurate correction.

Higher-order corrections for instrumental effects, such as uneven sampling in wavelength space, and spectroscopic effects, such as atmospheric absorption and the Ring effect, may eventually be developed if analysis of flight data indicates that they are warranted.

This research was funded by the National Aeronautical and Space Administration and the Smithsonian Institution. We thank Marcel Dobber and Ruud Dirksen of the Koninklijk Nederlands Meteorologisch Instituut (Royal Dutch Meteorological Institute) and Ruud Hoogeveen of the Stichting Ruimte Onderzoek Nederland (Space Research Organisation of the Netherlands) for help with information on GOME and OMI detector responses and ITF determinations. It is always a pleasure to acknowledge the European Space Agency and the German Aerospace Center for their ongoing cooperation in GOME and SCIAMACHY.

References

1. European Space Agency, *The GOME Users Manual, European Space Agency Publication SP-1182*, F. Bednarz, ed. (European Space Agency, Noordwijk, The Netherlands, 1995).
2. K. Chance, "Analysis of BrO measurements from the Global Ozone Monitoring Experiment," Geophys. Res. Lett. **25,** 3335–3338 (1998).
3. K. V. Chance and R. J. D. Spurr, "Ring effect studies: Rayleigh scattering, including molecular parameters for rotational Raman scattering, and the Fraunhofer spectrum," Appl. Opt. **36,** 5224–5230 (1997).
4. S. Slijkhuis, A. von Bargen, W. Thomas, and K. Chance, "Calculation of undersampling correction spectra for DOAS spectral fitting," in *Proceedings of the European Symposium on Atmospheric Measurements from Space* (1999), pp. 563–569.
5. K. Chance, P. I. Palmer, R. J. D. Spurr, R. V. Martin, T. P. Kurosu, and D. J. Jacob, "Satellite observations of formaldehyde over North America from GOME," Geophys. Res. Lett. **27,** 3461–3464 (2000).
6. R. V. Martin, K. Chance, D. J. Jacob, T. P. Kurosu, R. J. D. Spurr, E. Bucsela, J. F. Gleason, P. I. Palmer, I. Bey, A. M. Fiore, Q. Li, and R. M. Yantosca, "An improved retrieval of tropospheric nitrogen dioxide from GOME," J. Geophys. Res. **107,** 4437, doi:10.1029/2001JD0010127 (2002).
7. NASA, *OMI Algorithm Theoretical Basis Document Volume 4: Trace Gas Algorithms*, K. Chance, ed., (2002), http://eospso.gsfc.nasa.gov/eos_homepage/for_scientists/atbd/.
8. S. Goldman, *Information Theory* (Prentice-Hall, N.Y., 1953).
9. R. W. Hamming, *Digital Filters* (Prentice-Hall, Englewood Cliffs, N.J., 1977).

10. J. C. Brasunas, Jr., "Far-infrared spectroscopy of gaseous nebulae," Ph.D. dissertation (Department of Physics, Harvard University, 1981).
11. J. E. Murray, "Atlas of the spectrum of a platinum/chromium/neon hollow-cathode reference lamp in the region 240–790 nm," ESA Report (European Space Agency, 1994).
12. M. Dobber and R. Dirksen, Koninklijk Nederlands Meteorologisch Instituut, Wilhelminalaan 10, 3732 GK, De Bilt, The Netherlands (personal communication, 2003).
13. C. Caspar and K. Chance, "GOME wavelength calibration using solar and atmospheric spectra," in *Proceedings of the Third ERS Symposium on Space at the Service of our Environment*, T.-D. Guyenne and D. Danesy, eds., European Space Agency publication SP-414 (European Space Agency, 1997).
14. R. Spurr and W. Thomas, "GOME software databases for level 1 to 2 processing," ER-TN-IFE-GO-0018, Iss./Rev.3/A (2002), http://earth.esa.int/services/esa_doc/doc_gom.html.
15. W. E. Blass and G. W. Halsey, *Deconvolution of Absorption Spectra* (Academic, N.Y., 1981).
16. C. E. Sioris, C. S. Haley, C. A. McLinden, C. von Savigny, I. C. McDade, W. F. J. Evans, J. C. McConnell, N. D. Lloyd, E. J. Llewellyn, D. Murtagh, U. Frisk, T. P. Kurosu, K. V. Chance, K. Pfeilsticker, H. Bösch, and F. Weidner, "Stratospheric profiles of nitrogen dioxide observed by Optical Spectrograph and Infrared Imager System on the Odin satellite," J. Geophys. Res. **108,** 4215, doi:10.1029/2002JD002672 (2003).
17. W. H. Press, P. B. Flannery, S. A. Teukolsky, and W. A. Vetterling, *Numerical Recipes* (Cambridge University Press, Cambridge, UK, 1986).
18. H. K. Roscoe, D. J. Fish, and R. L. Jones, "Interpolation errors in UV-visible spectroscopy for stratospheric sensing: implications for sensitivity, spectral resolution, and spectral range," Appl. Opt. **35,** 427–432 (1996).